



Mechanical response and failure pattern of a modified mixed compression-shear experiments based on acoustic emission and numerical simulation

Tao Wei¹ · Chaolin Wang¹ · Daguo Quan¹ · Jing Bi¹

Received: 16 October 2023 / Accepted: 28 January 2024 / Published online: 9 March 2024
© The Author(s), under exclusive licence to Springer-Verlag GmbH Germany, part of Springer Nature 2024

Abstract

There is potential danger of conical shear failure surface in karst cave roof under pile foundation load. To understand the mechanical and failure characteristics of rocks under such conditions. In this study, an auxiliary device consisting of an indenter and a hollow support combined with a servo-controlled mechanical equipment was used to perform mixed compression-shear tests. The laboratory tests were studied numerically by finite difference methods. This study set up 4 groups of height variables 20, 30, 40, 50 mm and 3 groups of aperture variables 20, 30, 40 mm. AE (acoustic emission) tests are adopted to study the failure characteristics of specimen. The experimental results show that the peak load increases with the sample height while decreases with the aperture of support. This paper defines an apparent elastic modulus in terms of displacements and loads, which increases with height by 42.12, 51.7, and 49.00 KN/mm for apertures from 20 to 40 mm. The AE data show that the ratio of RA (ratio of rise time to maximum amplitude) to AF (average frequency of AE count) gradually increases as the support aperture increases, indicating that the aperture is approximately close to the radius of the indenter and that shear damage is approximately significant. The numerical simulation results show that the shear stress is the largest at the position where the upper surface of the specimen contacts with the indenter, and the displacement is the largest at the position where the lower surface of the specimen overlaps with the support hole. The extrusion phenomenon caused by dilatation is the main reason for the tensile failure detected during the experiment.

Keywords Rock mechanics · AE count · Compression-shear test · Failure pattern

Introduction

Mixed compression-shear failure often occurs in rock slopes, tunnel engineering and mining engineering. The shoulder of underground cavern is prone to compressive shear effect under overlying load. Karst cave roof also has similar phenomenon. A large number of scholars have studied the stability of the karst roof under pile load (Yang et al. 2021; Cao et al. 2022; Jiang et al. 2011; Meng et al. 2012; Wu et al. 2021). When there is a karst cave under the bedrock at the pile end, punching shear failure, shear failure or compression-shear failure may occur in the rock mass (Wu et al. 2019a, b; Jiang et al. 2008; Feng et al. 2020). The direct

shear test is widely used in the laboratory to obtain the shear strength of samples. This method mainly has two forms: box-type direct shear test and punch shear test (Xu et al. 2019). The International Society for Rock Mechanics recommends that box-type direct shear tests are carried out to obtain the compressive shear strength of intact rocks (Meng et al. 2019), rock joints (Cui et al. 2021; Li et al. 2019; Qi et al. 2020; Saiang et al. 2005), concrete interfaces (Tian et al. 2014). Huang and Zhu (2019) modified the shear box, conducted shear tests on rock under tensile action by means of cementation. Park et al. (2013) proposed a new constitutive model to describe the shear behavior of rock joints under constant normal stiffness and constant normal load conditions. Morad et al. (2019) investigated the effect on slip velocity and geometrical evolution of the initially rough limestone surfaces, and the results show that an increase in shear rate will result in an increase in roughness and shear stiffness. Huang et al. (2022) conducted a study on the propagation of compression-shear fracture by coupling effects

✉ Chaolin Wang
chaolinwang@126.com

¹ College of Civil Engineering, Guizhou University, Huaxi District, Guiyang 550025, Guizhou, China

of confining pressure and crack surface friction. The result shows that compared with confining pressure, surface friction contributes more inference on the fracture propagation after crack closure.

In order to study the characteristics of shear failure, AE technology is often used to monitor the characteristics of AE signals in shear tests (Yang et al. 2022; Chen et al. 2022; Du et al. 2021; Meng et al. 2020; Chen and Zhao 2020). Usually, one AE signal corresponds to the generation of a microcrack (Meng et al. 2020). Dense AE event numbers or high-energy AE signals are used to capture the occurrence of macroscopic rock failure (Zhai et al. 2021; Du et al. 2020). Numerous studies have tended to apply AE for estimating the sudden occurrence of shear failure and identifying failure patterns (Wu et al. 2019a, b; Shen et al. 2019; Meng et al. 2021; Wang et al. 2021; Yang et al. 2020), the analysis of parameter RA and AF was used for crack type determination. The analytical method or numerical method is able to reveal the stress state in the process of specimen failure (Zhao et al. 2020, 2022), which can comprehensively reflect the mechanism of rock failure in combination with the AE characteristics.

The punch shear test was originally used to test the shear strength of rock. Auxiliary equipment and rock disk specimens were combined, staggered and put into a compression testing machine for testing to obtain the shear strength. Some scholars have studied the influence of loading rates on shear strength by placing similar auxiliary devices under the Hopkinson bar (Xia and Yao 2015; Lukić and Forquin 2016; Huang et al. 2020). Punch tests can be divided into conventional punch shear test (PS), block punch test (BPS), and punch through shear test (PTS) according to the type of indenter or the slotting of rock disks (Mishra and Basu 2012; Huang et al. 2011). Punching shear test has the advantage of simple operation, but cannot reflect the effect of compressive stress on shear failure.

Conventional shear devices are not capable of studying the damage characteristics of conical shear surfaces. To understand the deformation and damage characteristics of the cavern roof under the circular pile foundation. In this study, we made simple modifications to the auxiliary devices in the punch shear test. A length less than or equal to the indenter diameter of 4 cm is taken to make the inner diameter of the hollow support to obtain the compression-shear or direct shear effect. A series of laboratory and numerical simulations were carried out on sandstone. The organizational structure of this paper is as follows. After the introduction of Sect. "Introduction", the auxiliary shear device and experimental process are introduced in Sect. "Experimental preparation". The test results including failure mode of rock specimen, AE

signal, and maximum shear stress distribution are discussed in Sect. "Experimental results and discussions". Sect. "Numerical investigation" presents the numerical tests and results of the compression-shear tests. Conclusions of the study are presented in Sect. "Conclusions".

Experimental preparation

A modified mixed compression-shear test method consisting of a set of auxiliary devices (which includes a cylindrical indenter and a perforated support) is developed (as shown in Fig. 1) to simulate the preset angle shear test (PAS). The indenter radius R_1 is greater than (or equal to) that of the inner diameter R_2 of the circular hole in the support. Note that the direct shear (DS) case occurs when R_1 equals R_2 .

The tested samples are red sandstone which are collected from Changsha, Hunan Province, China. The main mineral components of the tested samples are SiO_2 , quartz, feldspar, calcite, and dolomite. The average density of the specimens is 2197.3 kg/m^3 . Cylindrical specimens were prepared with a diameter of 75 mm. The height of the specimen ranges from 20 to 50 mm. Table 1 lists the formation of the tested specimens. These specimens were named according to the following rules. The first two symbols indicate the sample height, while the last two symbols represent the diameter of perforated support. For example, Sample H2Y2 represents the specimen with a height of 20 mm and is used for shear test on the condition of diameter of perforated support $R_2 = 20 \text{ mm}$.

Table 2 lists the basic mechanical parameters of red sandstone. The uniaxial compressive strength of the red sandstone is 33.05 MPa and the elasticity modulus of elasticity was 6.29 GPa. Brazilian splitting tests were conducted on four identical specimens to obtain the tensile strengths. The average tensile strength of the tested specimens is 0.89 MPa. The cohesive force of the sandstone specimen is about 2.966 MPa and the internal friction angle is about 44.727° .

A rock mechanics testing system is used to perform the pressure shear test. The testing system composes of three parts: data acquisition and processing system, stress loading system, and pore-pressure loading systems (see Fig. 1). The system has a maximum axial force of 1000 kN, and a maximum horizontal loading capacity of 200 kN. During the tests, AE events were monitored through a PAC's PCI-II AE acquisition system. The sampling frequency of the AE system was set to 1 MHz, and the main amplifier was set to 40 dB.

Fig. 1 Diagram of experimental system

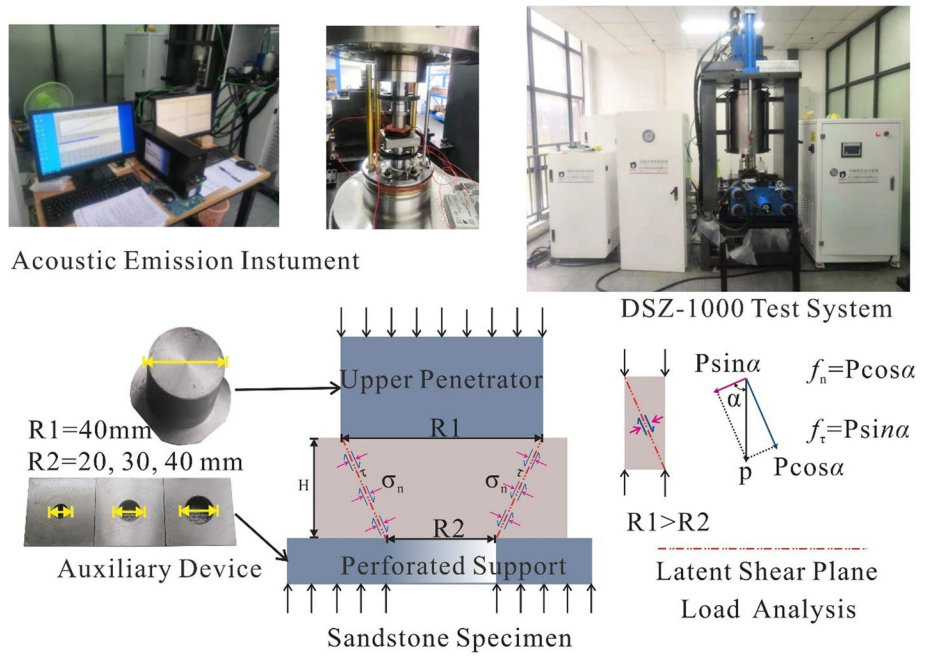


Table 1 Size information of tested specimens

Group number	Specimen number	Specimen height (mm)	Diameter of hollowed pedestal (mm)
Group1	H2Y2	20	20
	H2Y3		30
	H2Y4		40
Group2	H3Y2	30	20
	H3Y3		30
	H3Y4		40
Group3	H4Y2	40	20
	H4Y3		30
	H4Y4		40
Group4	H5Y2	50	20
	H5Y3		30
	H5Y4		40

Experimental results and discussion

Mechanical response and failure mode

Mechanical behavior of specimens with different base aperture sizes

Figure 2 shows the displacement–load curve of specimens with different base aperture sizes at 20, 30, 40 and 50 mm heights. There are similar characteristics in the load–displacement curves of specimens with different aperture sizes corresponding to each height. The load–displacement curves are composed of the compaction stage, the linear elastic stage, the plastic stage and the instability stage. Some curves also have a first stress drop stage and a subsequent stress drop stage. It can be seen from the figure that the strength of specimens under the 20 mm aperture base is always the highest, followed by

Table 2 Basic mechanical parameters of sandstone

Specimen	P (g/cm ³)	σ_c (MPa)	E (GPa)	μ (-)	σ_t (MPa)	C (MPa)	Φ (°)
Red Sandstone	2.1973	33.05	6.29	0.319	0.89	2.966	44.727

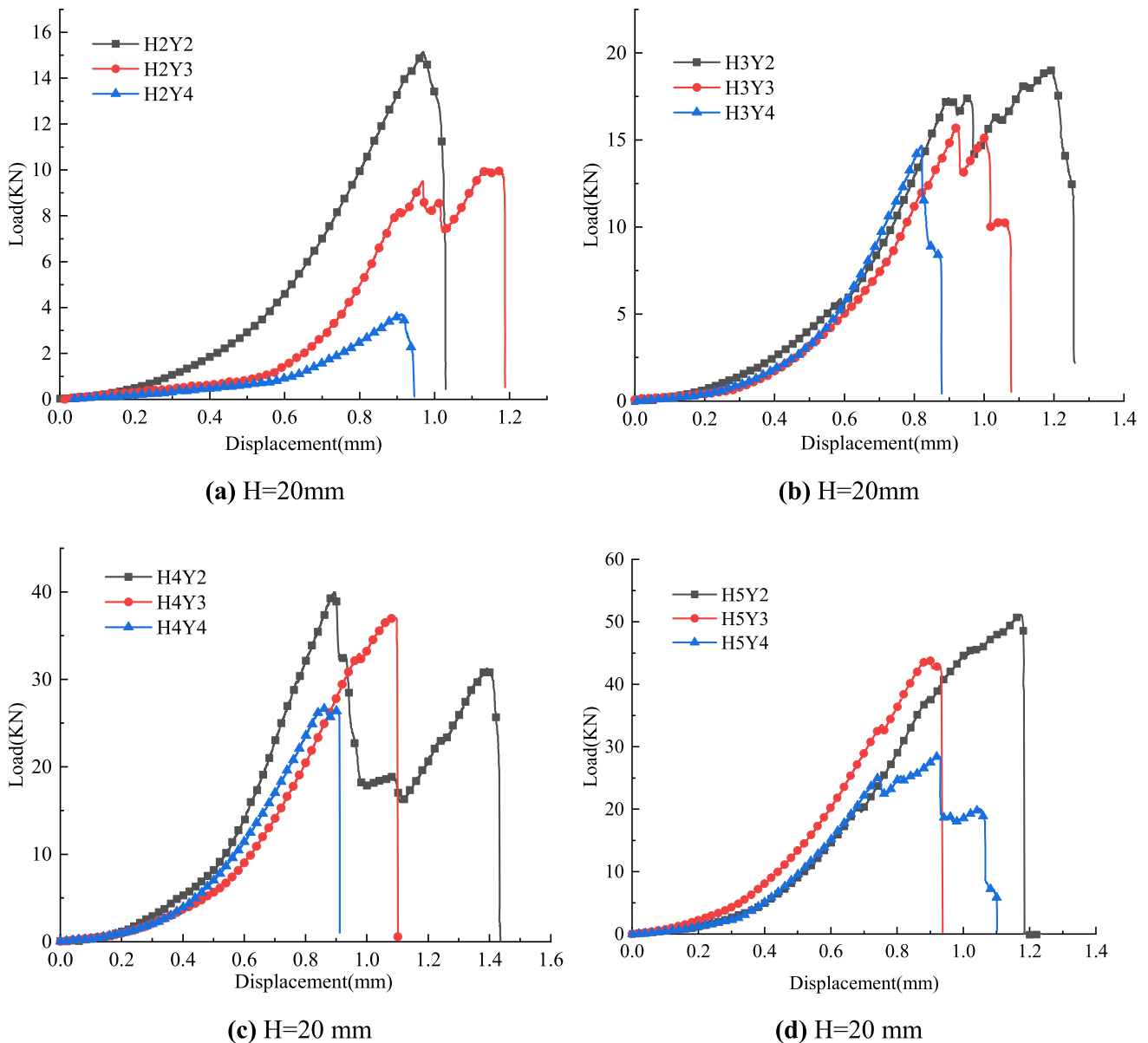


Fig. 2 Displacement–load curve of different aperture sizes with specimen heights of (a–d)

30 mm aperture, and the 40 mm aperture is the lowest. The reason is that in the case of specimens of the same height, as the aperture of base is larger, the effective bearing area of the base to specimen is smaller, which makes the specimen more prone to failure.

The relationship between the peak load of the specimen and the aperture size of the base can be obtained by fitting by the least square method. In Fig. 3 the correlation coefficients of fit curve all reached above 0.9, indicating that the peak specimen load showed a good negative correlation with the base

aperture at the same height. The load strength of the specimen with a height of $H=20$ mm ultimately decreases by 75.52% when the base aperture increases from 2 to 4 cm. Similarly, for specimens with heights of $H=30$, 40, and 50 mm, the load strengths decrease by 23.22%, 33.27%, and 44.21% respectively. When the specimen height $H=20$ mm, the load strength of the specimen exhibits its most significant decrease with an increase in the base aperture size, indicating that the overall strength is predominantly influenced by the dimensions of the base aperture when dealing with smaller specimen heights.

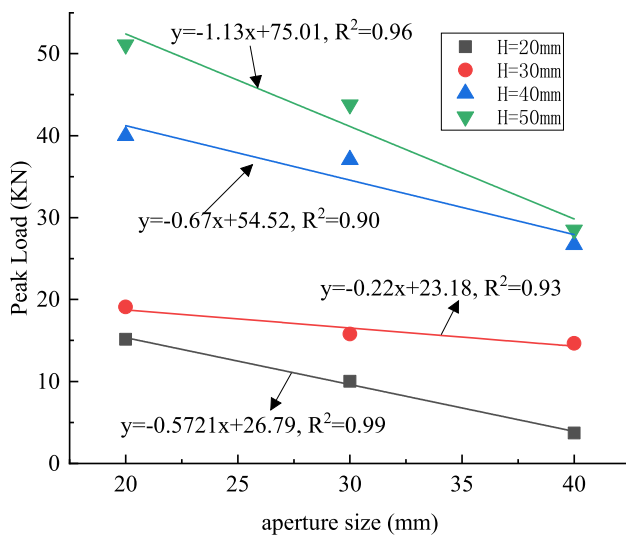


Fig. 3 Fitting curves of aperture size vs. peak loading

Mechanical behavior of specimens with different heights

Figure 4 shows the influence of different heights on the strength characteristics of specimens with the same base aperture. Overall, the heights of the specimen and the load strength of the specimen showed a positive correlation. The apparent elastic modulus, defined as the ratio of load difference to displacement difference in the elastic phase, demonstrates a consistent increase with increasing specimen height.

To investigate the effect of different heights on the strength characteristics of sandstone specimens with 20 mm, 30 mm and 40 mm aperture, the peak strength and specimen height were fitted, and the fits are shown in Fig. 5. When the correlation coefficient R_2 of the fitted curve is greater than 0.8 indicates that the fit is reliable, so the above fit is satisfactory. The peak load increased as the specimen height increased while keeping the base aperture size constant. This is attributable to the increase in the area of the potential shear surface within the sandstone specimen as the height of the specimen increases, with a corresponding increase in the bearing area. Under the influence of a 20 mm base aperture, the peak load of the specimen increases by 237.19%; under a 30 mm base aperture it increases by 336.71%; and under a 50 mm base aperture, it increases by 668.55%. This indicates that as the hole size of the base becomes larger, damage is more likely to occur in the specimen and there is greater sensitivity to changes in peak load.

It is worth noting that as shown in Fig. 6, exhibiting a positive correlation with different specimen heights, the slopes of the apparent elastic modulus change slightly with different base apertures, and the intercepts of the fitted straight lines tended to increase approximately linearly with increasing base aperture size. The change in support aperture from 20 to 40 mm corresponds to an increase in apparent elastic modulus of 42.12, 51.70, and 49.00 KN/mm, respectively.

The load–displacement curves of two typical specimens are analyzed. The first type of load–displacement curve is shown in Fig. 7a, which is represented by H5Y2. According to the characteristics of the curve, it can be divided into four stages: compaction stage (OA), elastic stage (AB), plastic stage (BC) and post-peak failure stage (CD). Another type of load–displacement curve is shown in Fig. 7b, which is represented by H5Y2. It also can be divided into four stages: compaction stage (OA), elastic stage (AB), stress fluctuation stage (BC), and final failure stage (CD).

The main difference between the two curves is after the elastic phase. The main difference between the two curve characteristics is in the section (BC). During this period the microfractures within the rock mass expand cumulatively, and once the load reaches the ultimate strength the specimen is immediately destabilized. For the second type of curves, stress fluctuation occurs after point B, which is mainly caused by the formation of localized damage and stress redistribution in the shear process.

Failure patterns of specimens

The damage morphology of the rock is an important feature for characterizing its damage mechanism. Figure 8 shows the morphology of tested specimens. After the compression–shear tests, the sandstone specimen were broken into several blocks, including a rock ring surrounding the shear plane and the core column. During the shear process, the rock annular body is likely to undergo radial fracture due to dilatancy, as shown in Fig. 8. A conical failure surface is formed for most specimens except for specimens with the case of $R_2 = 40$ mm. For specimens with the same height, the shape of core column evaluates from half cone to cylinder as R_2 increases from 20 to 40 mm. Meanwhile, the broken pieces of the rock ring decreases with the base diameter R_2 . For specimens tested with the same base condition, the failure modes are relatively complex for specimens with higher height. Specimens with height of 50 mm may not form a complete conical failure surface, and contain multiple failure

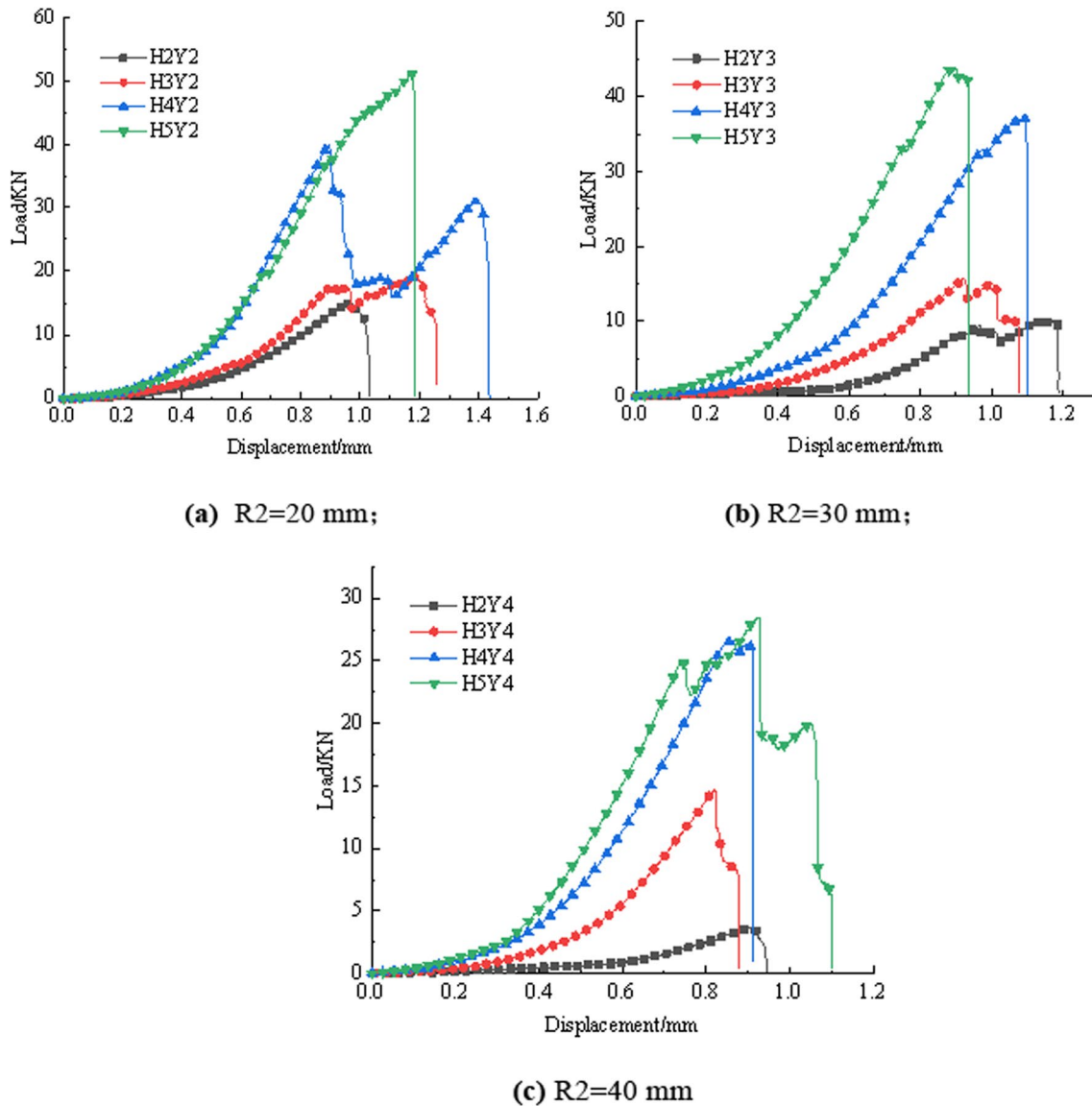


Fig. 4 Displacement–load curve of different specimen heights at the base aperture sizes of (a–c)

surfaces in the direction of diameter. This can be attributed for two reasons. First, the compression stress on the shear plane is not uniformly distributed, and the non-uniform stress increases with the sample height, resulting in a complex stress condition. Second, the rock ring surrounding the shear plane provides the stiffness condition (not the load

condition). The amount of rigidity provided by the rock ring depends on the thickness of the rock ring. In this test, the rock annular body is of non-uniform thickness and increases the specimen height. Therefore, the specimens with height of 50 mm has a higher rigidity making it difficult to form a conical failure surface.

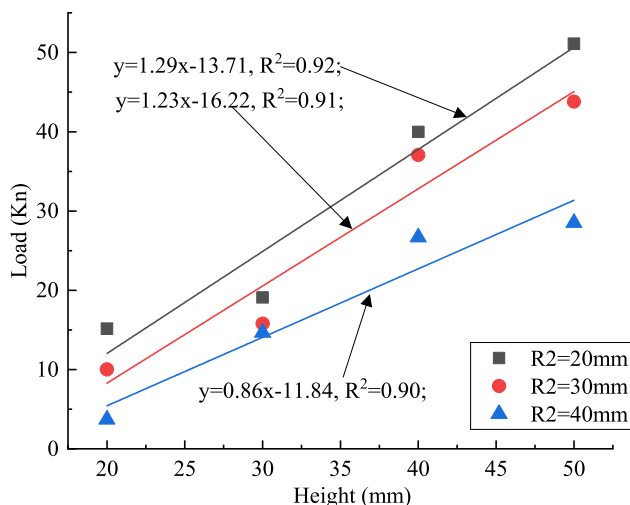


Fig. 5 Fitting curves of specimen height vs. peak loading

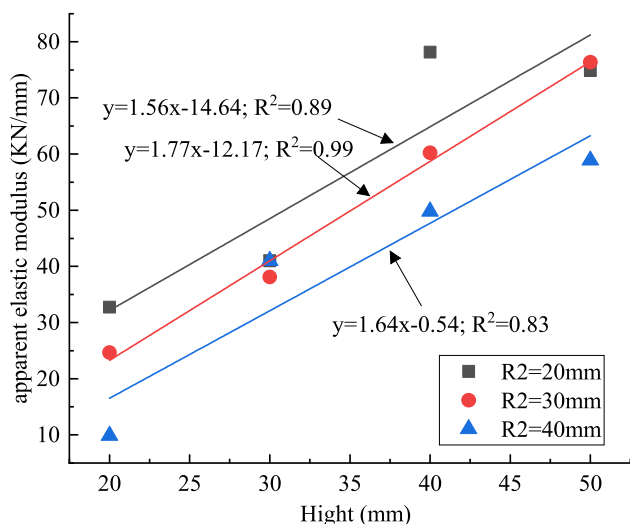


Fig. 6 Fitting curves of specimen height vs. peak loading

Study of AE characteristics of sandstone

This section analyzes the characteristic parameters of AE in the damage process of sandstone under different sets of conditions, and explores the variation pattern of AE during compression and shear, to understand the development of cracks and the damage law within the damaged sandstone specimens. Mainly analyze the relationship between AE ringing counts, cumulative ringing counts and load–displacement curves, and the types of crack damage are also discussed.

Parametric analysis was used for crack type determination. The RA value is the ratio of rise time to maximum amplitude in AE parameters, while the average frequency AF is the ratio of AE count to duration time, calculated as follows.

$$R_A = \frac{\text{Raise time}}{\text{Amplitude}}, \tag{1}$$

$$A_F = \frac{\text{Ring count}}{\text{Duration time}}. \tag{2}$$

As shown in Fig. 9, the dashed line is the dividing line to distinguish tension and shear cracks. Specifically, the data points above the line represent tension cracks and the data points below the line refer to shear cracks. The generation of tension cracks is often accompanied by AE signals with low R_A and high A_F values, while the generation of shear cracks is accompanied by AE signals with high R_A and low A_F values (Shiotani et al. 2001).

The values of R_A and A_F were obtained by combining the AE characteristic parameters during the modified compression-shear test to classify the cracks and to analyze the crack evolution process.

AE characteristics of specimens with different heights

The AE ringing count can characterize the damage evolution inside the rock specimen, and the cumulative ringing count characterizes the cumulative damage inside the specimen (Zhang et al. 2023a, 2023b). Figure 10 shows the curves of the load, ringing count, and cumulative ringing count with time for sandstone specimens with varied height ($R_2 = 20$ mm). The figure shows that the AE ringing counts all appear as a peak point at some point in time, and there are obvious fluctuations before and after the peak point. In addition, compared with specimens with a height of $H = 20$ mm, ringing counts of specimens with heights of $H = 30, 40$ and 50 mm reached the peak later, indicating that $H = 20$ mm specimens show simple damage models and are more likely to be sheared. The number of AE ringing meters for the $H = 50$ mm specimen is much larger than other specimens. This indicates that the damage pattern of the specimen is more complex, which also explains why the failure modes of specimens with a height of 50 mm in Fig. 3 are more complex than the other height specimens.

Figure 11 shows the scatter distribution of AE R_A – A_F for sandstone specimens with different heights. In general, the

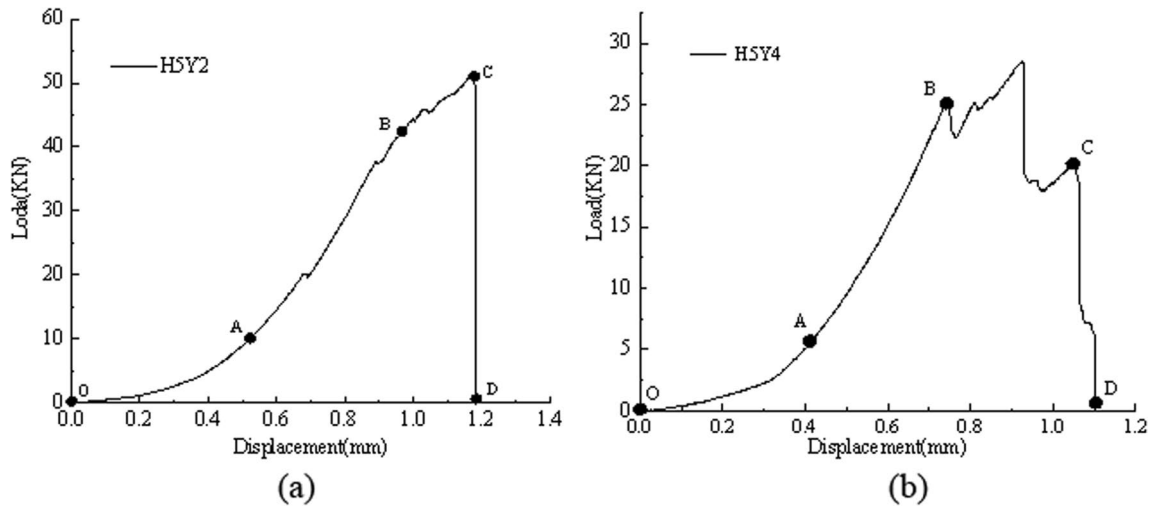


Fig. 7 Load–displacement characteristic curve with case of a H5Y2 and b H5Y4

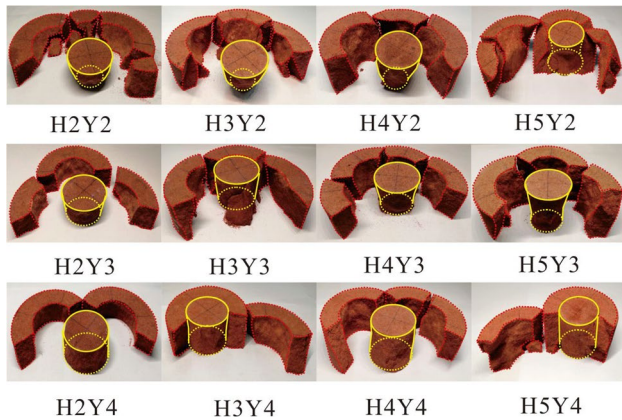


Fig. 8 Failure patterns of specimens

R_A – A_F data are mainly concentrated in the tensile crack area, which indicates that the cracks are mainly tensile cracks. With the increase of specimen height, the data with low A_F values and high R_A values gradually decrease, indicating that the proportion of shear cracks gradually decreases. During loading, the upper part of the specimen is damaged first. With the increase of specimen height, the non-uniform stress increases, and shear damage may not occur along the potential shear surface, resulting in a decrease of the proportion of shear cracks.

AE characteristics of specimens with different heights

Figure 12 shows the AE characteristic curves corresponding to different base apertures of specimens with a height

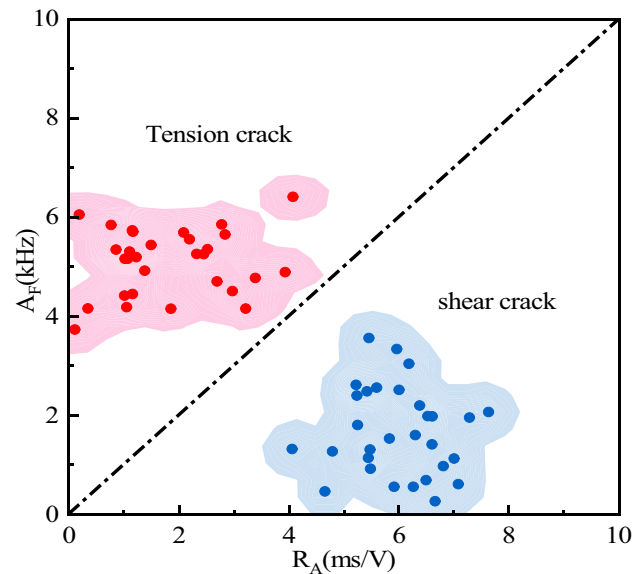


Fig. 9 Crack classification method based on R_A and A_F values

of 30 mm. These curves all have an obvious feature. Compared with the load–displacement curve, the ringing count corresponding to the impending stress drop will suddenly increase, and the greater the fall amplitude, the greater the number of ringing counts.

Comparing ringing count curves under different base aperture conditions, it can be found that all ringing count curves start to mutate at about 500 s, and with the increase of base aperture, the mutation time of curves is

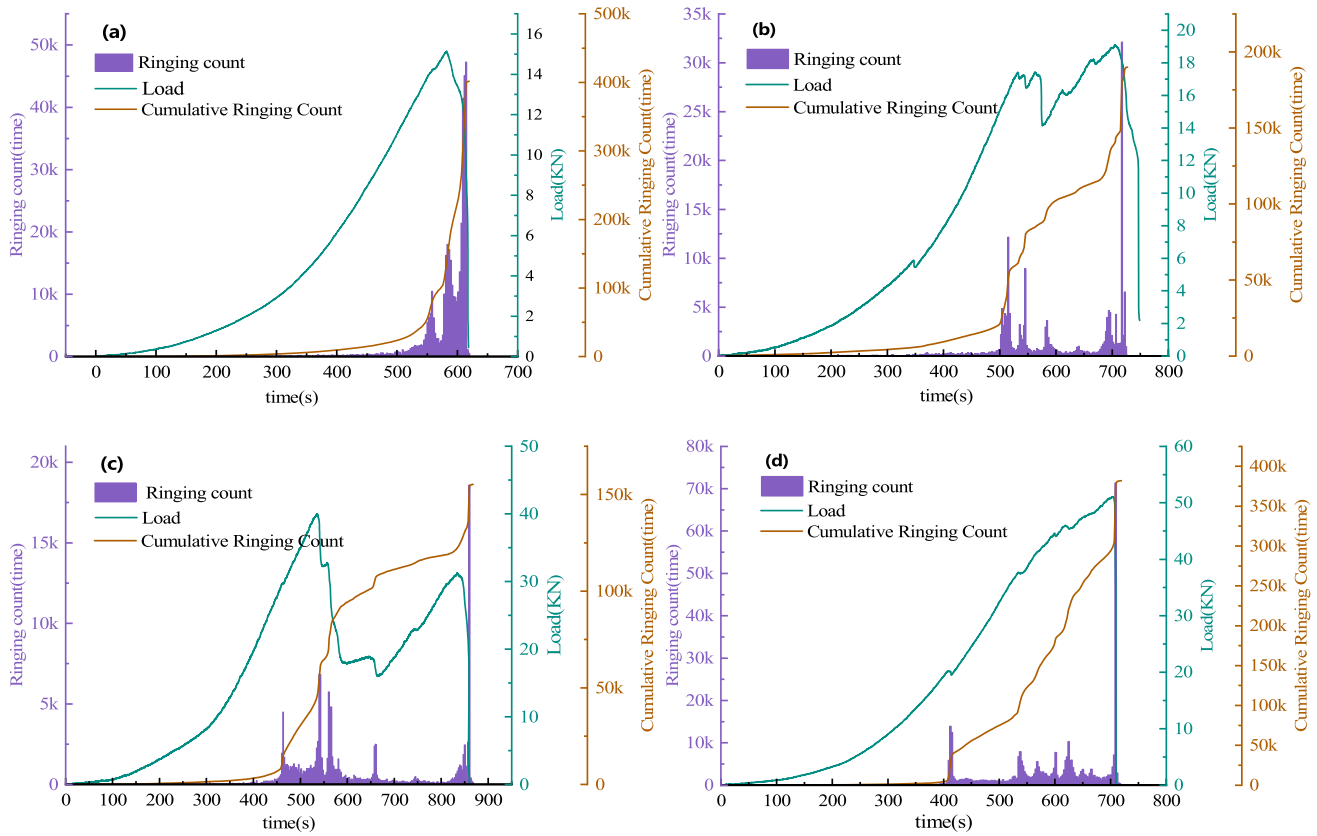


Fig. 10 Curves of load, ringing count and cumulative ringing count versus time of specimen with varied height **a** $H=20$ mm **b** $H=30$ mm; **c** $H=40$ mm; and **d** $H=50$ mm

also significantly advanced, while the period of sudden increase of cumulative ringing count decreases. It shows that the direct shear is accompanied by a large number of microcracks, and once the macroscopic failure occurs, a large amount of strain energy is released immediately. For compressive shear, the energy release process is relatively slow after the rock reaches yield strength, and the energy dissipation rate decreases with the decrease of aperture diameter.

Figure 13 shows the scatter distribution of AE R_A-A_F of sandstone specimens (with height of 30 mm) under different base diameters. With the increase of R_2 , it is found that the cracks in the tension region change little, but the R_A-A_F data in the shear region gradually increase, indicating that the percentage of shear cracks increases gradually with R_2 .

Numerical investigation

Numerical model and parameter setting

To further investigate the internal stress, displacement and damage evolution characteristics of sandstone specimens during the compression-shear process with perforated supports. A series of numerical simulation tests were conducted using FLAC3D. The mechanical parameters are obtained from the laboratory tests in Table 2. Similarly, the numerical simulation consists of three main components, the bottom restraint, the specimen, and the upper load. The specimens consist of $20 \times 20 \times 20 \times 4$ cylinder units with a 37.5 mm radius (as shown in Fig. 14). The z-direction of the bottom restraint is fixed to zero. The upper load is applied at a velocity of 2×10^{-7} mm/step in the z-direction.

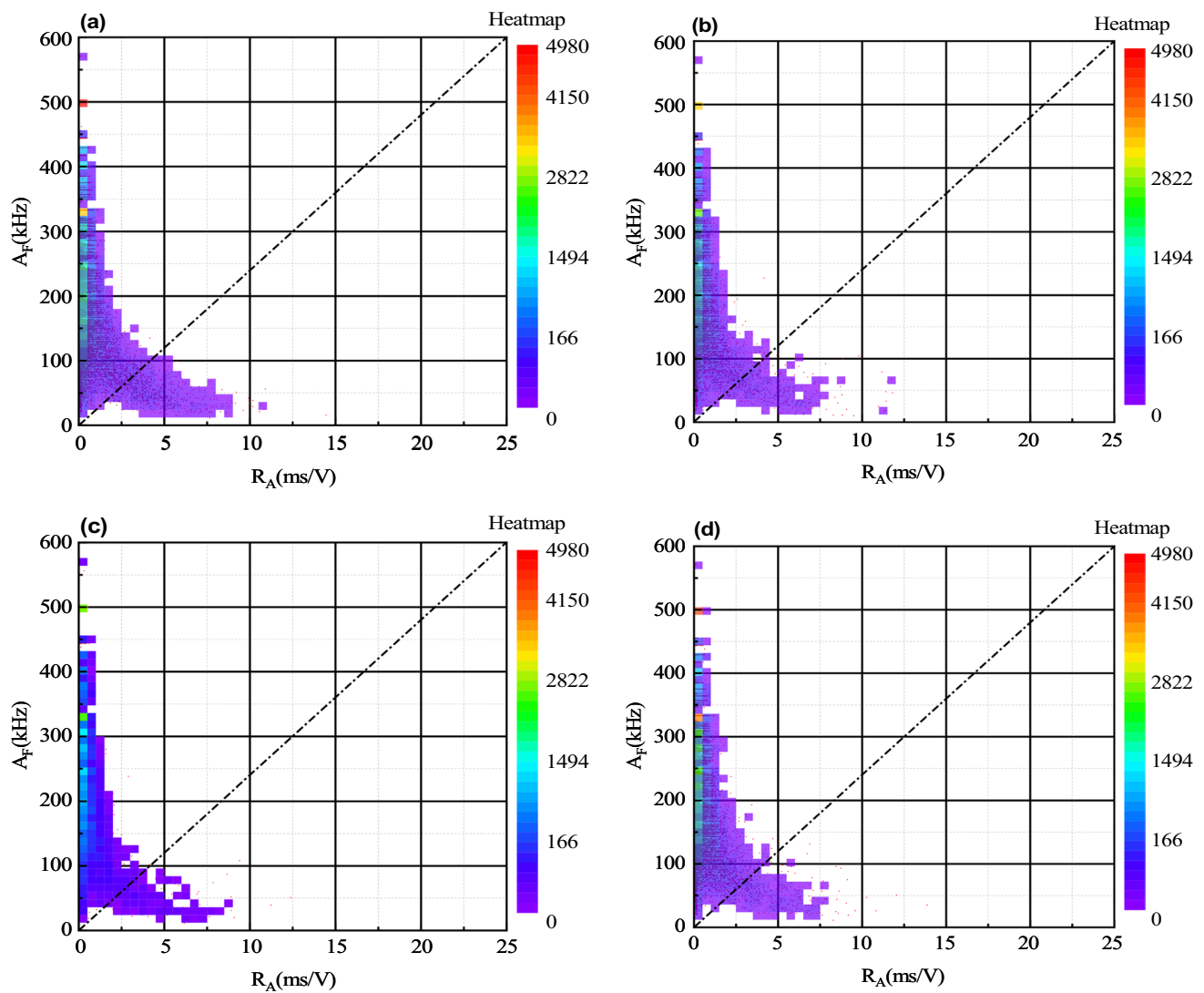


Fig. 11 The scatter distribution of AE R_A – A_F of sandstone specimens with varied heights. **a** $H=20$ mm; **b** $H=30$ mm; **c** $H=40$ mm; and **d** $H=50$ mm

To describe the mechanical behavior of these specimens, the Hooke's law in terms of the generalized stress and stress increments was adopted. The failure envelope for this model corresponds to a Mohr–Coulomb criterion (shear yield function) with tension cutoff (tension yield function). The position of a stress point on this envelope is controlled by a non-associated flow rule for shear failure, and an associated rule for tension failure. It can effectively identify the failure mode of micro-elements in shear tests.

Numerical simulation results

For shear tests, shear stress distribution characteristics should be the first thing to be concerned with. Figure 15 shows the maximum shear stress contour of the specimens. Maximum principal shear stress principal distribution along the potential shear surface. The upper surface of the specimen in the figure shows a concentration of shear stresses, which is the area most susceptible to shear

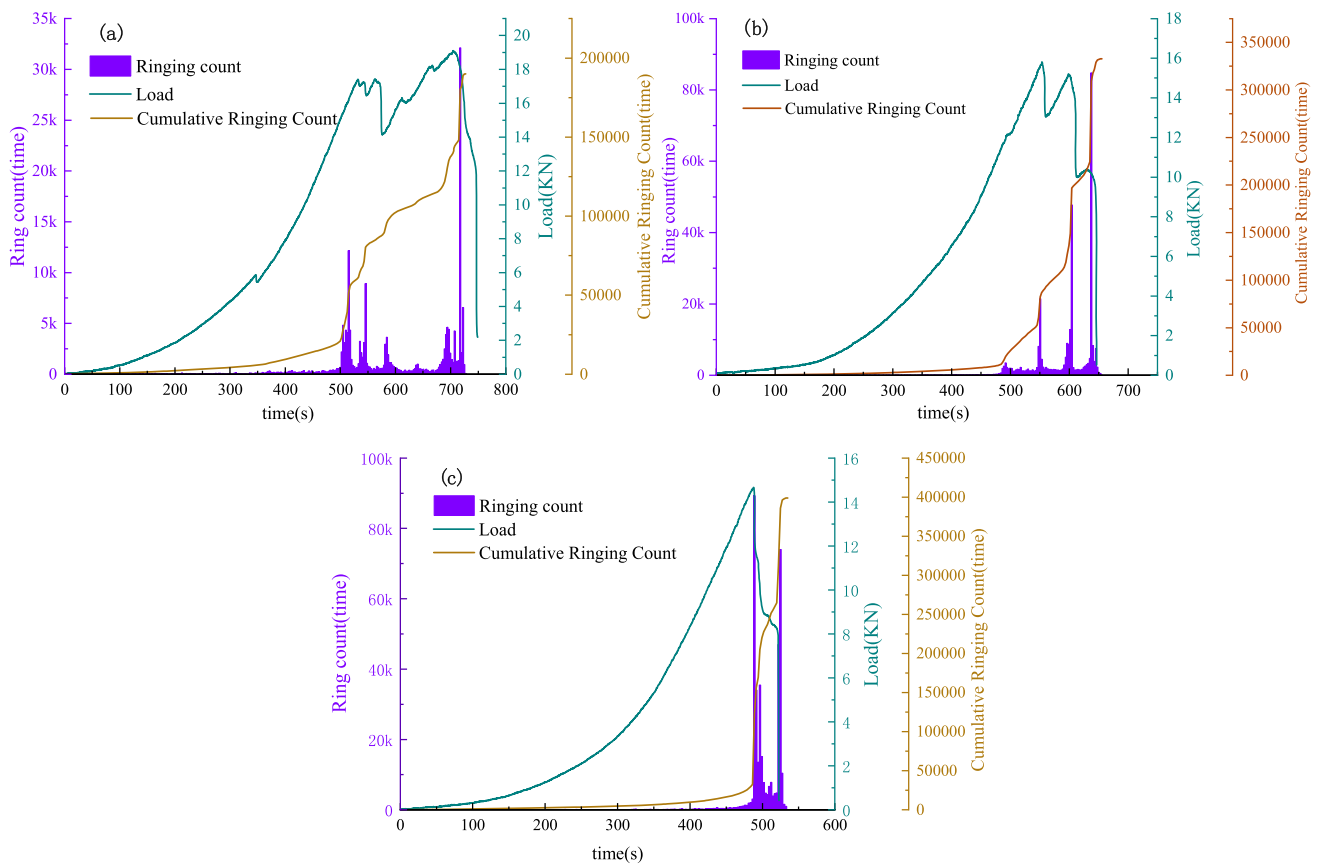


Fig. 12 Variation curves of load, ringing count and cumulative ringing count with time under base aperture size of **a** $R_2=20$ mm; **b** $R_2=30$ mm; **c** $R_2=40$ mm

damage. To further investigate the shear stress characteristics of the specimens under different combination conditions, the peak shear stress of each specimen was collected. The relationship between specimen height and bearing aperture and maximum shear stress was discussed by best linear fitting. The fitting coefficients R^2 were all greater than 0.86.

Figure 16 demonstrates the evolution of the maximum shear stress in the potential shear surface with the base aperture for different specimen heights. Firstly, it can be seen that as the base aperture increases, all groups of specimens show a negative correlation with maximum shear stresses. When the height of the specimen was changed from 20 to 50, the corresponding maximum shear stresses decreased by 1.77, 1.47, 1.24 and 0.39, respectively. The reduction decreases as the height of specimens increases. On the one hand, the increase of the aperture of the base reduces the shear separation Angle. Under such conditions, the smaller

Mohr circle can meet the Coulomb shear failure criterion, so the maximum shear stress is reduced. On the other hand, as the height of the specimen increases, the friction area increases, so a greater shear stress is required to cause the specimen to break.

To further study the deformation and failure characteristics of compressive shear behavior, we selected group H4Y3 for further study. (The selection principle is: Avoid direct shear damage ($R_2=40$ mm), and the value of the variable is close to the median). Figure 17 shows the load–displacement dotted lines recorded by H4Y3 in laboratory and numerical simulations. It can be seen that the characteristics of the two curves do not coincide, but the peak load and displacement are roughly the same. Because the numerical simulation assumes that the rock is intact without cracks, there is no compaction process, and macro failure occurs after linear stage and yield stage. In general, the analysis of numerical model is reliable.

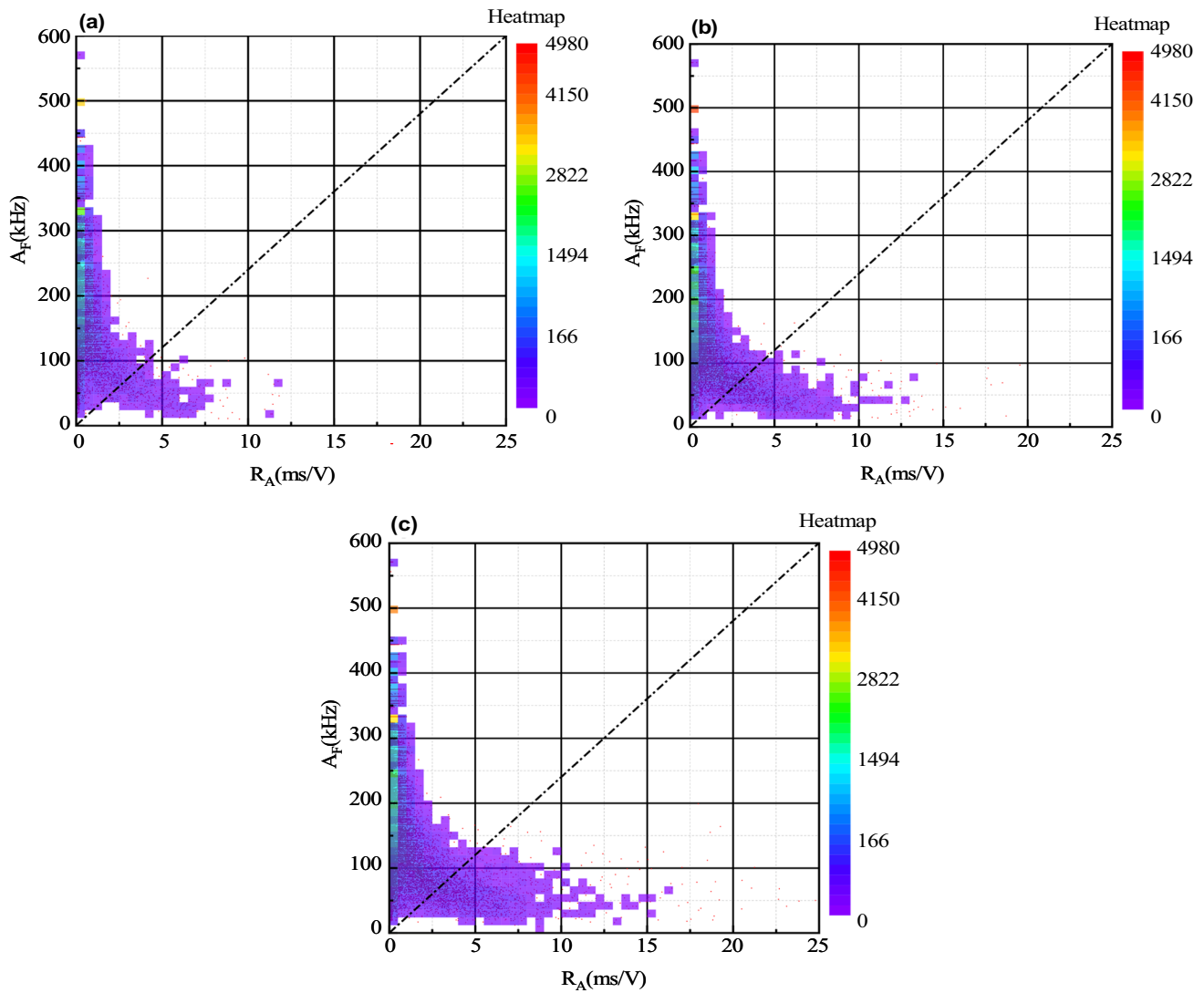


Fig. 13 The scatter distribution of AE R_A – A_F of sandstone specimens under different base diameters **a** $R_2=20$ mm; **b** $R_2=30$ mm; and **c** $R_2=40$ mm

Figure 18 shows the Z-direction displacement evolution curve of the monitoring points in the shear process, which are evenly distributed on the potential shear plane. It can be seen that the lower the position of the monitoring point, the slower the rate of displacement increase, indicating that the deformation on the shear plane is not uniform. The position near the load is easy to produce damage first. At 6000step, the displacement in the z-direction of the monitoring point is 1.2, 1.16, 0.94, 0.47, 0 mm from top to bottom.

Figure 19 shows the nodal displacements of the H4Y3 specimen during loading. The maximum displacements occur at the indenter and then propagate downward. The nodal displacement occurs mainly inside the potential slip surface with the displacement direction downward. When the load exceeds 1000 step, the nodes in the lower part of the specimen started to show a tendency to move outward. This phenomenon indicates that normal displacement will occur when the specimen slides along the potential failure surface under load, and such "shear-dilation" effect is more

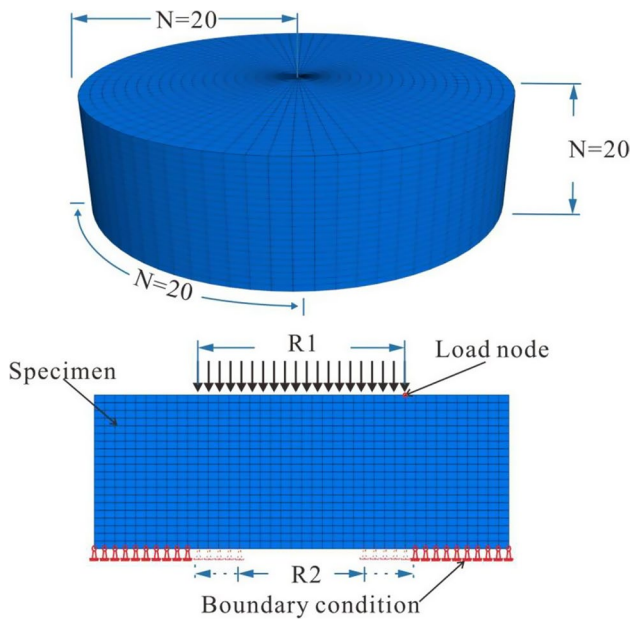


Fig. 14 The numerical model

obvious at the bottom of the specimen. This tendency causes an increase in the hoop tensile stress in the region of the specimen outside the slip plane, which explained the reason why there is a lot of tensile-shear damage monitored in the AE test. Since the tensile strength of the rock is relatively low, the peripheral area of the specimen is easily pulled off in the test, which is verified in the laboratory test results.

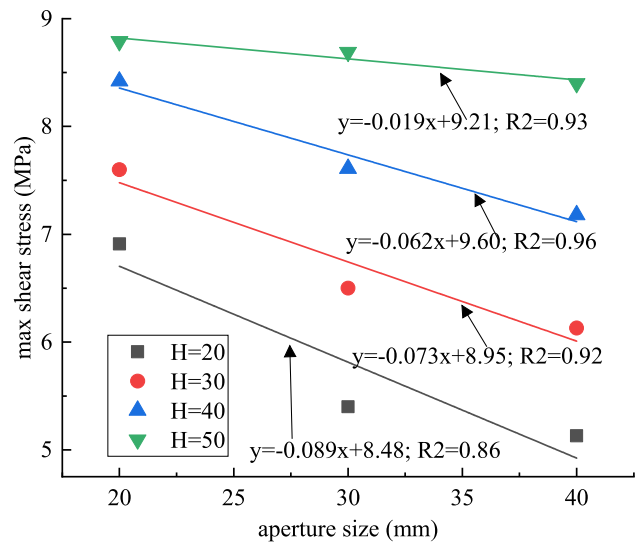


Fig. 16 Fitting curves of aperture size vs. max shear stress

The shear-tension composite failure criterion is adopted in this simulation, shear and tension represent two failure modes, and the suffixes ' -n 'and' -p 'represent current and historical stress states. When the load reaches 2000 steps, there are some tensile failure at the bottom of the specimen, which is mainly caused by the formation of a gap in the aperture of the support. Under the action of the upper load, these nodes tend to be extruded, thus resulting in tensile failure. However, these tensile cracks did not cause

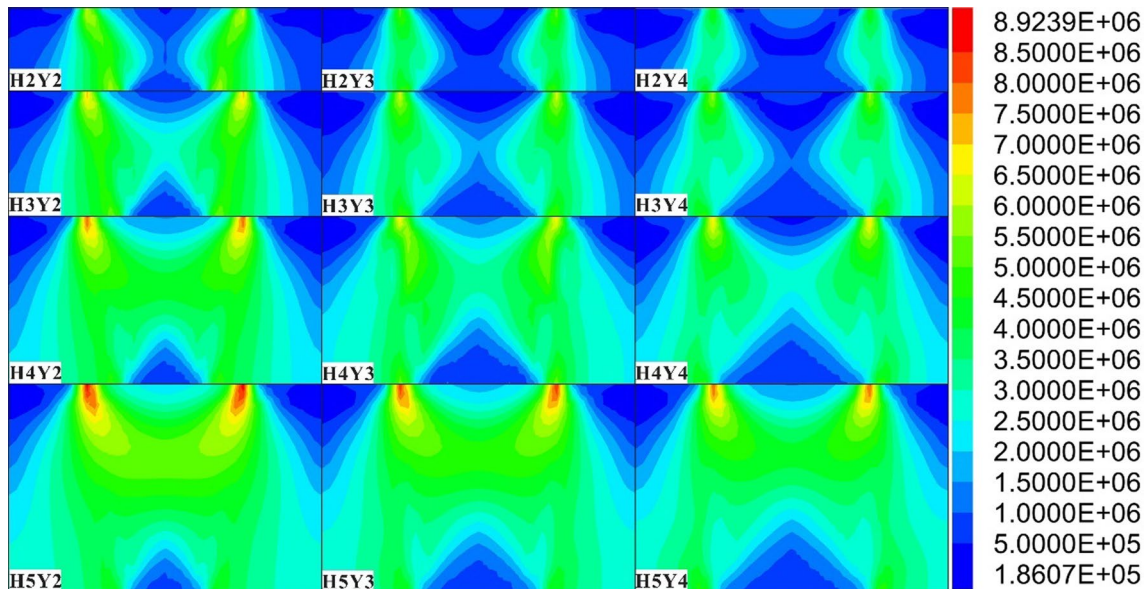


Fig. 15 Contour plot of maximum shear stress of the specimens

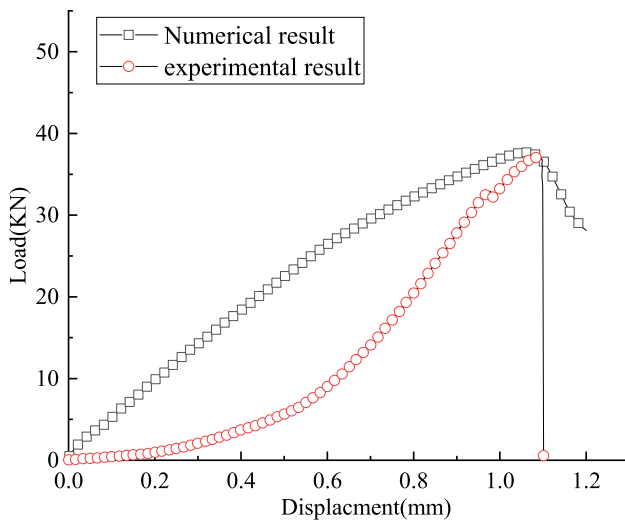


Fig. 17 Load– displacement curves recorded in laboratory and numerical data

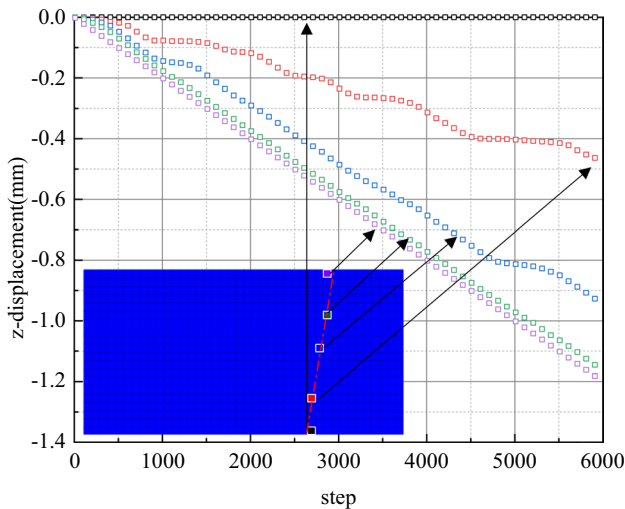


Fig. 18 Displacement curve of the monitoring point on the shear surface of H4Y3 specimen

macroscopic damage in the laboratory, which may be one of the reasons for detecting low energy AE signals in the early stage of the experiment. At 3000 steps, shear failure begins to occur at the inner diameter of the indenter and the support, At 5000 steps, the shear fracture is transfixed on the slip plane (see Fig. 20). Then a shear failure zone was formed in the lower part of the specimen and outside

the slip plane, and finally a circle of tension cracks was formed outside the specimen. In some test results in Fig. 8, fragments were generated in the shear failure zone, indicating that the shear cracks were partially transfixed in the shear failure zone. At the same time, the tensile crack produced in the late simulation verifies the conclusion that in the displacement analysis, the circumferential tensile stress is produced due to "shear dilation", which leads to the tensile failure of the specimen periphery.

Conclusions

In this study, compression-shear tests were implemented using a perforated support aid to study the strength characteristics and damage modes of specimens with different support apertures and specimen heights, during which AE equipment was used to monitor the test process for the damage mechanism study of sandstone. The numerical simulation software FLAC3D was used to study the optimum stress distribution, displacement behavior and failure evolution of the specimens. The following conclusions can be drawn from this research work:

(1) The peak strength on the specimen increases with the height of the specimen, and the increase in the size of the hole inside the base will lead to a decrease in the peak strength of the specimen. The apparent modulus of elasticity showed a negative correlation with increasing base aperture diameter and a positive correlation with increasing specimen height.

(2) The increase in height of the specimen makes the integrity of the internal circular or cylindrical block produced by the damage of the specimen decrease, while the increase in the size of the base hole will make the overall fragmentation of the specimen decrease, and the damage mode will change from compression-shear damage to pure shear damage.

(3) With the increase of hole diameter of the support, the number of RA-AF data points in the shear region gradually increases, indicating that the proportion of shear cracks gradually increases.

(4) The shear stress is the largest where the upper surface of the specimen is in contact with the indenter, and the displacement is the largest where the lower surface of the specimen coincides with the aperture of the support. The radial displacement caused by shear expansion is the main cause of tensile failure.

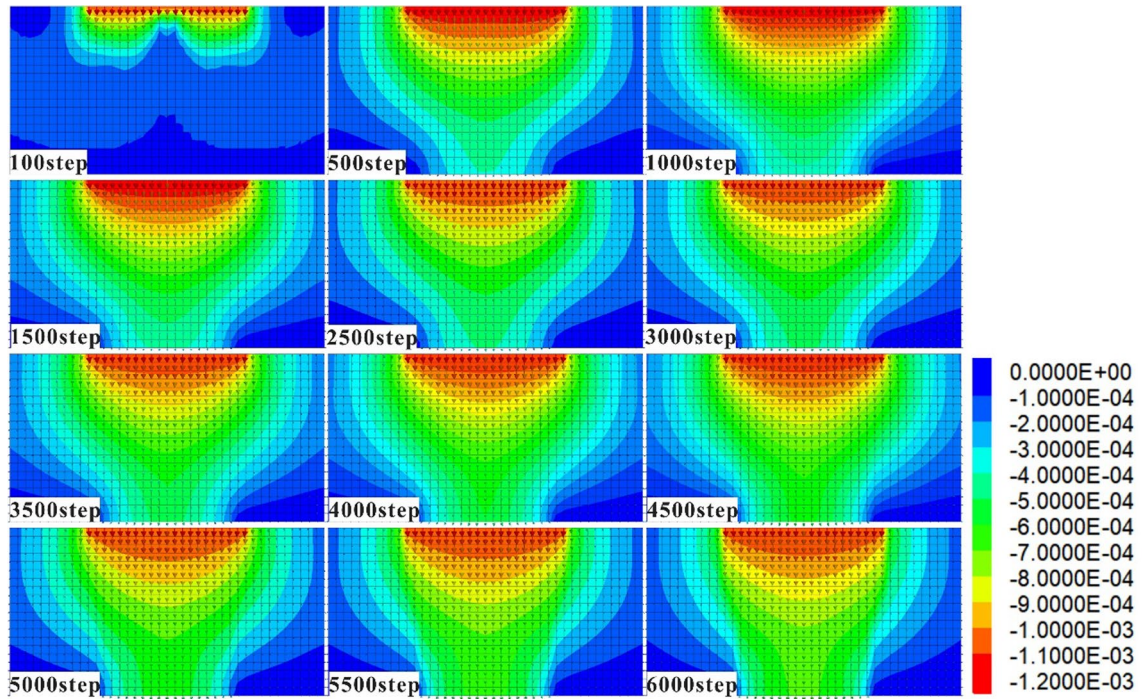
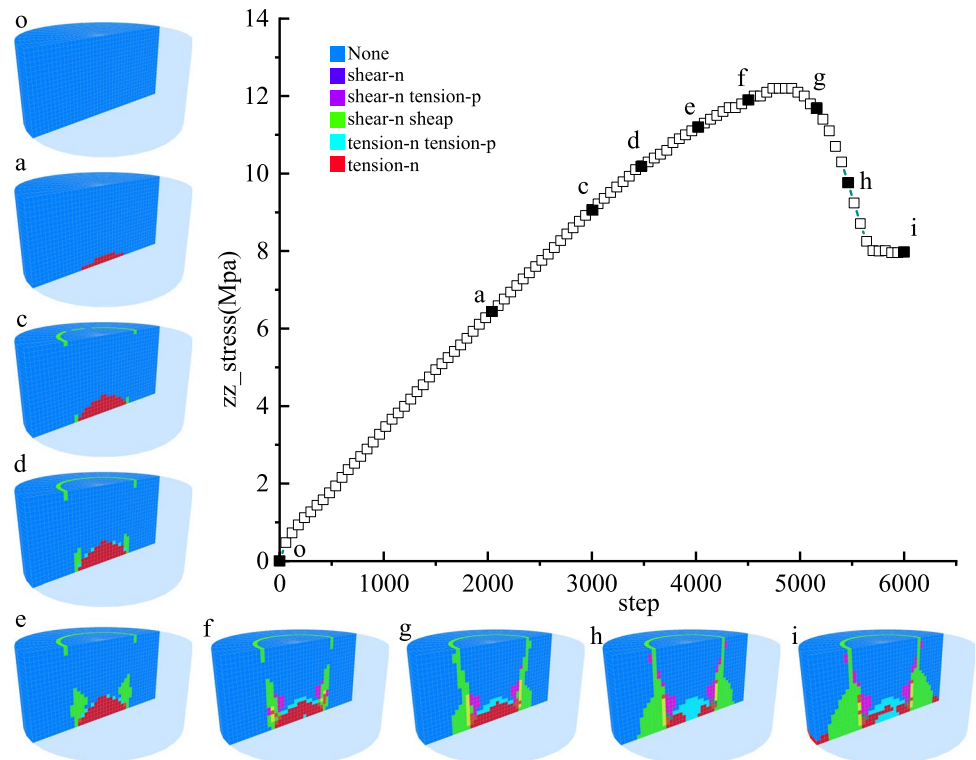


Fig. 19 Displacement contour map and displacement vector evolution of the H4Y3 specimen

Fig. 20 Element state evolution and zz_stress vs step curve of slip surface



Author contributions Tao Wei: writing—original draft preparation. Chaolin Wang: conceptualization, methodology, data curation, and visualization. Daguo Quan: investigation, software, and validation. Jing Bi: writing—reviewing and editing.

Funding This research was supported by National Natural Science Foundation of China (No. 52004072, and No. 52164001), the Guizhou Provincial Science and Technology Foundation (No. [2021]292).

Declarations

Conflict of interest The authors declared that they have no conflicts of interest in this work. We declare that we do not have any commercial or associative interest that represents a conflict of interest in connection with the work submitted.

References

- Cao X, Tang H, Li H, Sun G (2021) Probability model for embedment of single pile into rock masses at building sites in karst terrain. *Arab J Geosci* 14(14):1–8
- Chen YD, Zhao ZH (2020) Correlation between shear induced asperity degradation and AE energy in single granite fracture. *Eng Fract Mech* 235:107184
- Chen T, Zhao K, Yan Y, Zhou Y, He Z, Guo L (2022) Mechanical properties and AE response of cemented tailings backfill under variable angle shear. *Constr Buil Mater* 343:128114
- Cui Z, Sheng Q, Zhang M, Cao J, Mei X, Luo Q (2021) A new direct shear apparatus for rock joints specialized in cyclic loading. *Rock Mech Rock Eng* 54(8):4321–4327
- Du K, Li XF, Tao M, Wang SF (2020) Experimental study on AE (AE) characteristics and crack classification during rock fracture in several basic lab tests. *Int J Rock Mech Min* 133:104411
- Du K, Li XF, Wang SY, Tao M, Li G, Wang SF (2021) Compression-shear failure properties and AE (AE) characteristics of rocks in variable angle shear and direct shear tests. *Measurement* 183:109814
- Feng Z, Chen J, He J, Huang Z, Dong Y, Jiang D, Meng Y (2020) Study on vertical bearing characteristics of bridge pile foundation in karst area considering the size. *IOP Conf Ser Mater Sci Eng* 780(2):022003
- Huang D, Zhu T (2019) Experimental study on the shear mechanical behavior of sandstone under normal tensile stress using a new double-shear testing device. *Rock Mech Rock Eng* 52(9):3467–3474
- Huang S, Feng XT, Xia K (2011) A dynamic punch method to quantify the dynamic shear strength of brittle solids. *Rev Sci Instrum* 82(5):053901
- Huang D, Cen D, Song Y (2020) Comparative investigation on the compression-shear and tension-shear behaviour of sandstone at different shearing rates. *Rock Mech Rock Eng* 53(7):3111–3131
- Huang J, Tang H, Pan X, Gan Z, Hua W, Dong S (2022) Investigation of the compression-shear fracture propagation for rocks accounting for confining pressure and crack surface friction. *Theoret Appl Fract Mech* 119:103346
- Jiang C, Zhao MH, Cao WG (2008) Stability analysis of subgrade cave roofs in karst region. *J Cent South Univ T* 15:38–44
- Jiang C, Li XB, Zhou KP, Wang SW (2011) A new reliability analysis method of karst roof under pile tip. *Appl Mech Mater* 90–93:133–136
- Li Y, Tang Ca, LiWu DC (2019) A new shear strength criterion of three-dimensional rock joints. *Rock Mech Rock Eng* 53(3):1477–1483
- Lukić B, Forquin P (2016) Experimental characterization of the punch through shear strength of an ultra-high performance concrete. *Int J Impact Eng* 91:34–45
- Meng Y, Lei M, Lin Y, Dai J, Guan Z (2012) Models and mechanisms of drilling-induced sinkhole in China. *Environ Earth Sci* 67(7):1961–1969
- Meng F, Wong LNY, Zhou H, Yu J, Cheng G (2019) Shear rate effects on the post-peak shear behaviour and AE characteristics of artificially split granite joints. *Rock Mech Rock Eng* 52(7):2155–2174
- Meng FZ, Wong LNY, Zhou H, Wang ZQ, Zhang LM (2020) Asperity degradation characteristics of soft rock-like fractures under shearing based on AE monitoring. *Eng Geol* 266:105392
- Meng YY, Jing HW, Liu XW, Yin Q, Wei XC (2021) Experimental and numerical investigation on the effects of bedding plane properties on the mechanical and AE characteristics of sandy mudstone. *Eng Fract Mech* 245:107582
- Mishra DA, Basu A (2012) Use of the block punch test to predict the compressive and tensile strengths of rocks. *Int J Rock Mech Min* 51:119–127
- Morad D, Hatzor YH, Sagy A (2019) Rate effects on shear deformation of rough limestone discontinuities. *Rock Mech Rock Eng* 52(6):1613–1622
- Park JW, Lee YK, Song JJ, Choi BH (2013) A constitutive model for shear behavior of rock joints based on three-dimensional quantification of joint roughness. *Rock Mech Rock Eng* 46(6):1513–1537
- Qi SW, Zheng BW, Wu FQ, Huang XL, Guo SF, Zhan ZF, Zou Y, Barla G (2020) A new dynamic direct shear testing device on rock joints. *Rock Mech Rock Eng* 53:4787–4798
- Saiang D, Malmgren L, Nordlund E (2005) Laboratory tests on shotcrete-rock joints in direct shear, tension and compression. *Rock Mech Rock Eng* 38(4):275–297
- Shen RX, Qiu LM, Zhao EL, Han X, Li HR, Hou ZH, Zhang X (2019) Experimental study on frequency and amplitude characteristics of AE during the fracturing process of coal under the action of water. *Safety Sci* 117:320–329
- Shiotani T, Ohtsu M, Ikeda K (2001) Detection and evaluation of AE waves due to rock deformation. *Constr Build Mater* 15(5–6):235–246
- Tian HM, Chen WZ, Yang DS, Yang JP (2014) Experimental and numerical analysis of the shear behaviour of cemented concrete-rock joints. *Rock Mech Rock Eng* 48(1):213–222
- Wang YY, Deng HC, Deng Y, Chen KP, He JH (2021) Study on crack dynamic evolution and damage-fracture mechanism of rock with pre-existing cracks based on AE location. *J Petrol Sci Eng* 201:108420
- Wu QH, Chen L, Shen BT, Dlamini B, Li SQ, Zhou YJ (2019a) Experimental investigation on rockbolt performance under the tension load. *Rock Mech Rock Eng* 52(11):4605–4618
- Wu J, Li S-C, Xu Z-H, Zhao J (2019b) Determination of required rock thickness to resist water and mud inrush from karst caves under earthquake action. *Tunnel Undergr Sp Technol* 85:43–55
- Wu QH, Weng L, Zhao YL, Feng f (2021) Influence of infilling stiffness on mechanical and fracturing responses of hollow cylindrical sandstone under uniaxial compression tests. *J Cent South Univ* 28(8):2485–2498
- Xia K, Yao W (2015) Dynamic rock tests using split Hopkinson (Kolsky) bar system—a review. *J Rock Mech Geotech Eng* 7(1):27–59
- Xu Y, Yao W, Xia K, Ghaffari HO (2019) Experimental study of the dynamic shear response of rocks using a modified punch shear method. *Rock Mech Rock Eng* 52(8):2523–2534
- Yang J, Mu ZL, Yang SQ (2020) Experimental study of AE multi-parameter information characterizing rock crack development. *Eng Fract Mech* 232:107045
- Yang Y, Li J, Liu C, Ma J, Zheng S, Chen W (2021) Influence of deep excavation on adjacent bridge piles considering underlying karst

- cavern: a case history and numerical investigation. *Acta Geotech* 17(2):545–562
- Yang B, Jiang Q, Feng X, Xin J, Xu D (2022) Shear testing on rock tunnel models under constant normal stress conditions. *J Rock Mech Geotech Eng* 14(6):1722–1736
- Zhai MY, Xue L, Chen HR, Xu C, Cui Y (2021) Effects of shear rates on the damaging behaviors of layered rocks subjected to direct shear: Insights from AE characteristics. *Eng Fract Mech* 258:108046
- Zhang Y, Zhao Y, Zang A, Long A (2023a) Acoustic emission evolution and hydraulic fracture morphology of changning shale stressed to failure at different injection rates in the laboratory. *Rock Mech Rock Eng*. <https://doi.org/10.1007/s00603-023-03586-8>
- Zhang Y, Long A, Zhao Y, Wang C, Wu S, Huang H (2023b) Impacts of wellbore orientation with respect to bedding inclination and injection rate on laboratory hydraulic fracturing characteristics of Lushan shale. *Fuel*. 353:129220
- Zhao Y, Wang CL, Bi J (2020) Analysis of fractured rock permeability evolution under unloading conditions by the model of elastoplastic contact between rough surfaces. *Rock Mech Rock Eng* 53(12):5795–5808
- Zhao Y, Wang C, Ning L, Zhao H, Bi J (2022) Pore and fracture development in coal under stress conditions based on nuclear magnetic resonance and fractal theory. *Fuel* 309:122112

Publisher's Note Springer Nature remains neutral with regard to jurisdictional claims in published maps and institutional affiliations.

Springer Nature or its licensor (e.g. a society or other partner) holds exclusive rights to this article under a publishing agreement with the author(s) or other rightsholder(s); author self-archiving of the accepted manuscript version of this article is solely governed by the terms of such publishing agreement and applicable law.